FULL PAPER

A High-Performance Binary Ni–Co Hydroxide-based Water Oxidation Electrode with Three-Dimensional Coaxial Nanotube Array Structure

*Zhenlu Zhao, Haoxi Wu, Haili He, Xiaolong Xu, and Yongdong Jin**

Developing nanostructured Ni and Co oxides with a small overpotential and fast kinetics of the oxygen evolution reaction (OER) have drawn considerable attention recently because their theoretically high efficiency, high abundance, low cost, and environmental benignity in comparison with precious metal oxides, such as RuO_2 and IrO_2. However, how to increase the specific activity area and improve their poor intrinsic conductivity is still challenging, which significantly limits the overall OER rate and largely prevent their utilization. Thus, developing effective OER electrocatalysts with abundant active sites and high electrical conductivity still remains urgent. In this work, a scrupulous design of OER electrode with a unique sandwich-like coaxial structure of the three-dimensional Ni@$[Ni^{(2+/3+)}Co_2(OH)_{6-7}]_x$ nanotube arrays (3D NNCNTAs) is reported. A Ni nanotube array with open end is homogeneous coated with Ni and Co co-hydroxide nanosheets ($[Ni^{(2+/3+)}Co_2(OH)_{6-7}]_x$) and is employed as multifunctional interlayer to provide a large surface area and fast electron transport and support the outermost $[Ni^{(2+/3+)}Co_2(OH)_{6-7}]_x$ layer. The remarkable features of high surface area, enhanced electron transport, and synergistic effects have greatly assured excellent OER activity with a small overpotential of 0.46 V at the current density of 10 mA cm^{-2} and high stability.

1. Introduction

Increasing energy demands have sparked intensive research on sustainable energy production and conversion systems with high efficiency, low cost, and environmental benignity, especially for water splitting.[1–3] Hydrogen, as an ideal clean fuel, has been considered as a promising alternative for traditional fossil fuels in the future,[4,5] however hydrogen production from electrocatalytic water splitting—one of the ideal hydrogen fuel producing methods—is limited by the slow kinetics of the oxygen evolution reaction (OER), imposing serious overpotential requirement.[6,7] OER is important in many energy conversion and storage technologies. However, OER is sluggish in nature and typically requires the use of expensive Ru and Ir-based catalysts. Despite recent advances in the development of various nanostructured heterogeneous catalysts to expedite the OER (Equation 5, where E_θ is the standard potential and NHE is the normal hydrogen electrode),[6,8,9] commercializing oxygen electrode catalysts with high activity at low cost remains a great challenge.

$$2H_2O(l) \rightarrow O_2(g) + 4H^+(aq) + 4e^- \qquad E^\theta(O_2/H_2O) = 1.23 \text{ V versus NHE} \qquad (1)$$

A major drawback to making these processes viable on an industrial scale is the inefficiency due to the kinetically sluggish of OER electrocatalysts.[10,11] Currently, although precious metal oxides,[12] such as RuO_2 and IrO_2, are the most effective electrocatalysts known for OER, they are not practical for large-scale applications because of their scarcity and high costs.[11] Therefore, an effective OER electrocatalyst that can expedite the reaction, reduce the overpotential, and thus enhance the energy conversion efficiency is highly desired. In response, non-noble metal-based catalysts, especially nickel (Ni) and cobalt (Co), have attracted growing research attention recently as a potential substitute for RuO_2 and IrO_2 owing to their earth-abundance, low cost, environmental benignity, and theoretically high catalytic activity, promoting the commercialization of oxygen electrode catalysts technology.[13–22] Although intensive research has been focused on developing high performance electroactive nanostructured Ni and Co oxides, we believe, for several reasons, that there is still considerable room for improvement in the synthesis and performances of nanostructured Ni- and Co- oxides for OER. Firstly, among many manufacture techniques, binder (polymer binder and conductive additives) is usually required; however, this pretreatment may reduce the specific activity area of OER electrode and result in poor electric conductivity, seriously poor stability, and sometimes the deterioration of the materials' structure. In contrast, electrodeposition process of the 3D NNCNTAs

Z. L. Zhao, H. X. Wu, H. L. He, X. L. Xu, Prof. Y. D. Jin
State Key Laboratory of Electroanalytical Chemistry
Changchun Institute of Applied Chemistry
Chinese Academy of Sciences
Changchun 130022, Jilin, P. R. China
E-mail: ydjin@ciac.ac.cn
Z. L. Zhao, H. X. Wu, H. L. He
University of Chinese Academy of Sciences
Beijing 100039, P. R. China

DOI: 10.1002/adfm.201400118

electrode by our proposed method could produce in situ OER electrode without the need for additional treatments. Secondly, previous studies and our work[23–28] showed that the various properties of the nanocomposite can be integrated and strongly enhanced by designing the structure of the nanocomposite. To further increase OER active sites and improve the electrocatalytic efficiency of OER, it is crucial to effectively increase the surface area for catalyst loading via structural design. A solution to this is using 3D and porous electrode materials structure. In addition, the Ni and Co co-existing electrocatalyst system may offer synergistic effect of Ni and Co on OER.[29,30] Therefore, inspired by the attractive electrocatalytic properties of the Co- and Ni-based oxides that reported recently,[1,31–37] it is expected that the Ni and Co co-existing electrocatalyst system may offer superb OER performance.

On the other hand, transition metal oxides including the Co- and Ni-based oxides, usually showed limited kinetics during the OER as a result of their low electrical conductivity and low surface area. Though the integration of Ni and Co hydroxides always possesses enhanced OER capability,[14,38] the overall performance is still unsatisfactory because of the poor intrinsic conductivity and short diffusion distance of electrolyte into OER electrodes, which makes the underneath parts hardly participate in the electrocatalytic process, leading to a less satisfactory the whole active surface.[29] An efficient design, for instance, is to directly grow the OER active materials on a porous nanostructured self-standing current collector in order to enhance the OER performance of Ni and Co hydroxides.[7,39,40]

Taking into account comparatively high surface area, high electron conductivity and low costs, the self-standing 3D NNCNTAs electrode for OER with coaxial nanotube array structure is firstly constructed electrochemically, in which Ni nanotube array with open end was homogeneous coated with Ni and Co co-hydroxide nanosheets ($[Ni^{(2+/3+)}Co_2(OH)_{6-7}]_x$) and was employed as multifunctional interlayer to provide a large surface area and fast electron transport and support the outermost $[Ni^{(2+/3+)}Co_2(OH)_{6-7}]_x$ layer. As a result of the effective utilization of the "core" and "shell" materials and their strong synergistic effects, the as-prepared self-standing 3D NNCNTAs electrode exhibits very good performance for OER. Specifically, this simple yet versatile strategy for the directly manufacture of OER electrode electrochemically reveals highly promising for many practical applications, such as in fuel cells, lithium-ion batteries, gas absorption, and supercapacitors.

2. Result and Discussion

The 3D NNCNTAs electrode which can be in situ applied to test the OER activity is facilely synthesized by a simple electrodeposition process, as illustrated in **Scheme 1**. The electrode fabrication method is described in the Experimental section in detail. Typical scanning electron microscopy (SEM) images showed that the morphology of the closely packed and well separated ZnO nanorods are uniform with an average diameter of about 300 nm and the thickness of about 1.5 μm (**Figure 1**a). The ZnO-Ni core-shell nanorod arrays were subsequently synthesized with an overall size of about 500 nm, as shown in Figure 1b. The Ni wraps were found preferentially deposited on the surfaces of the ZnO nanorods uniformly, and there are almost no Ni packed into the interspaces of the ZnO nanorods. After dissolving ZnO core, the discrete NNTAs with open end were obtained with maintained array structure (Figure 1c,d). The inner diameters and wall thicknesses of the resulting Ni nanotubes are about 300 and 100 nm, respectively. The corresponding chemical components of the electrode materials during the successive electrodeposition process were revealed and confirmed by elemental analysis of SEM energy dispersive spectroscopy (EDS) (Figure S1, Supporting Information). To verify the successful deposition of the Ni, we investigated

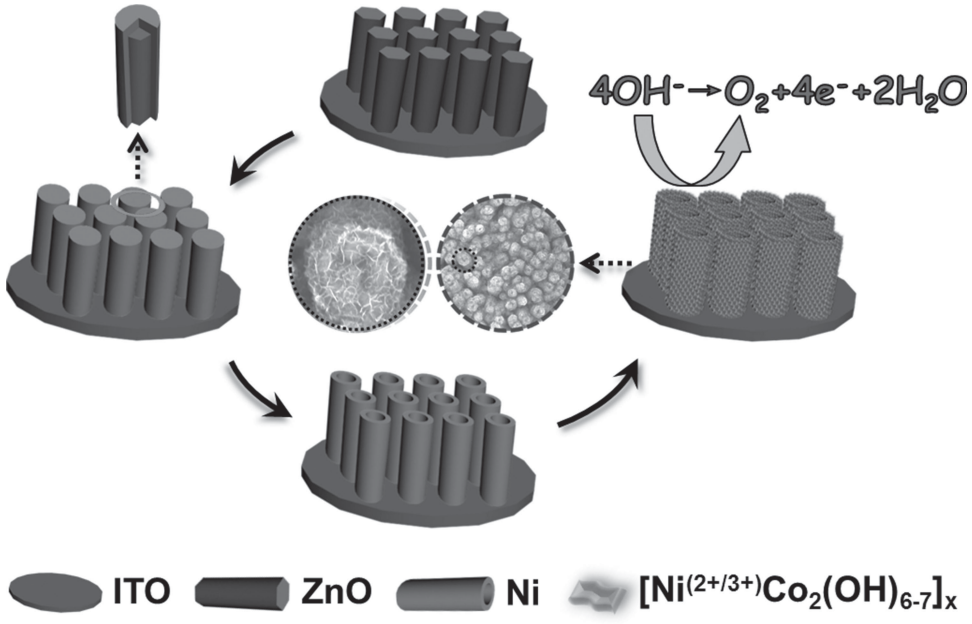

Scheme 1. Schematic illustration of the fabrication of the 3D NNCNTAs water oxidation electrode by means of electro-deposition.

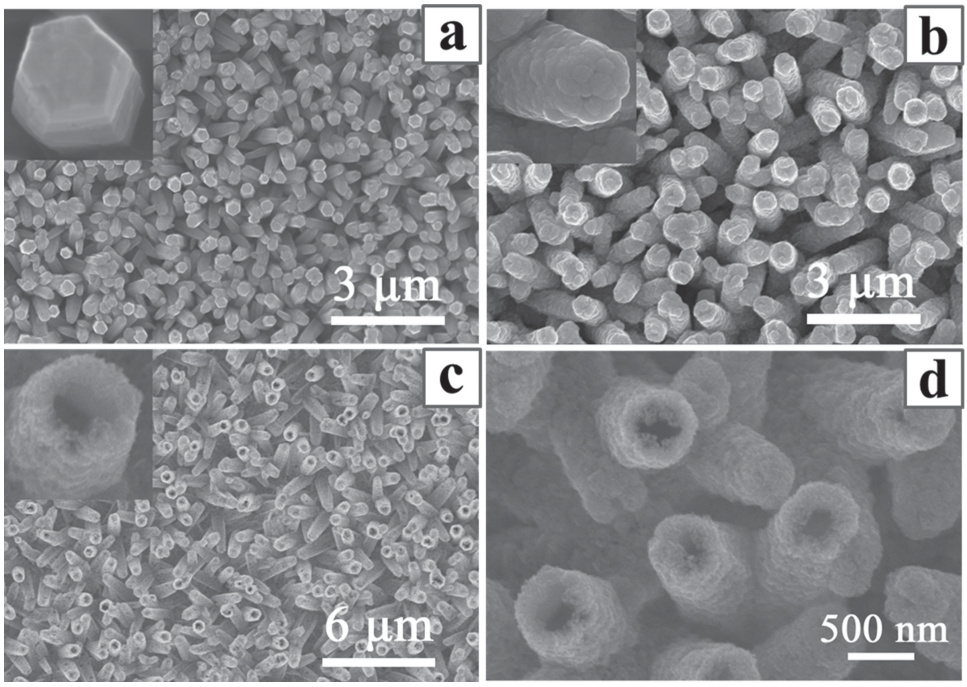

Figure 1. a) Typical SEM images of ZnO nanorod arrays, b) Ni-coated ZnO (ZnO–Ni) nanorod arrays, and c,d) etched Ni nanotube arrays (NNTAs) on ITO electrodes.

the X-ray photoelectron spectroscopy (XPS) result of Ni 2p of NNTAs. As expected, the Ni nanotube shows a Ni $2p_{3/2}$ peak at 852.1 eV and a Ni $2p_{1/2}$ peak at 869.5 eV, demonstrating the formation of metal Ni (Ni^0) nanotubes.[41,42] In addition, the result shows two spin-orbit doublets, characteristic of Ni^{2+} and Ni^{3+} and two shakeup satellites, which may be attributed to the partial oxidation of metal Ni. The as-prepared ITO-supported one-dimensional Ni (Ni^0) nanotubes due to their large surface area caused by open end and high void volume can serve as a favourable current collector. Therefore, it is expected to improve OER performance of the final 3D NNCNTAs with a unique sandwich like coaxial structures constructed on the basis of NNTAs. Through optimized electrochemical deposition, the $[Ni^{(2+/3+)}Co_2(OH)_{6-7}]_x$ deposited on the outer and inner surfaces of the Ni nanotube in a well-distributed manner to form sandwich-like nanotube arrays (**Figure 2** and Supporting Information Figure S2). As shown in typical transmission electron microscopy (TEM) images (Figure 2c,d), the dispersed coaxial nanotubes show a hollow morphology and the $[Ni^{(2+/3+)}Co_2(OH)_{6-7}]_x$ exhibits crystallinity as revealed by the high magnification TEM (HRTEM) images, which is in agreement with the X-ray diffraction (XRD) result. High magnification SEM images (Figure 2b and Supporting Information Figure S2f) show that the as-prepared $[Ni^{(2+/3+)}Co_2(OH)_{6-7}]_x$ nanosheets with a lateral size of several hundred nanometers are intercrossed with each other to form a nanosheet-like rippled silk texture, which creates loose porous nanostructures with abundant open space and electroactive surface sites.[43] The corresponding chemical component of the electrode materials was further confirmed by elemental analysis of EDS (Figure S1c, Supporting Information). Elemental mapping also reveals a uniform distribution of Ni and Co in the 3D NNCNTAs (Figure 2h,i), indicating the successful fabrication of the 3D NNCNTAs. This unique 3D porous morphology endowed by electrochemical deposition further improves the specific surface area and roughness factor of the OER active materials. This structural feature is expected to further enhance ionic conductivity and be favorable access to the electrolyte. We found experimentally that control of electrodeposition time is crucial to the formation of this feature. For longer electrodeposition time, the void spaces and interspaces of the nanotubes will be refilled, as revealed by a control sample (NNCNTAs-2) by using only double time (24 s) of Ni/Co co-electrodeposition under the same procedures and identical conditions (Figure S3 in the Supporting Information).

To better understand the detailed elemental composition and the oxidation state of the as-prepared 3D NNCNTAs electrode, we next employed XPS analysis and the corresponding results are presented in **Figure 3**. In the high-resolution O 1s region (Figure 3b), the 3D NNCNTAs display three oxygen peaks. Specifically, the peak at 531.7 eV is typical nickel–oxygen (Ni–O) bonds and the peak at 532.7 eV is cobalt–oxygen (Co–O) bonds,[39,43] and they are usually associated with oxygen in OH groups, indicating that the surface of the 3D NNCNTAs is hydroxylated to some extent as a result of either surface oxydroxide or the substitution of oxygen atoms at the surface by hydroxyl groups.[43,44] The component at 533.9 eV can be attributed to physic- and chemisorbed water at or near the surface.[39,43,45] In the Ni 2p region (Figure 3c), it was fitted with two spin-orbit doublets, characteristic of Ni^{2+} and Ni^{3+}, and two shakeup satellites.[39,43] In contrast, the Ni^{2+} and Ni^{3+} peaks (855.9 and 857.3 eV) of the 3D NNCNTAs shift to binding energies relative to the Ni^{2+} and Ni^{3+} peaks (855.2 and 856.4 eV) of Ni 2p of the Ni nanotube arrays (NNTAs) electrode (Figure 3a,c). As similar with previous studies,[20,46,47] the significant positive shifts (≈0.7 eV)

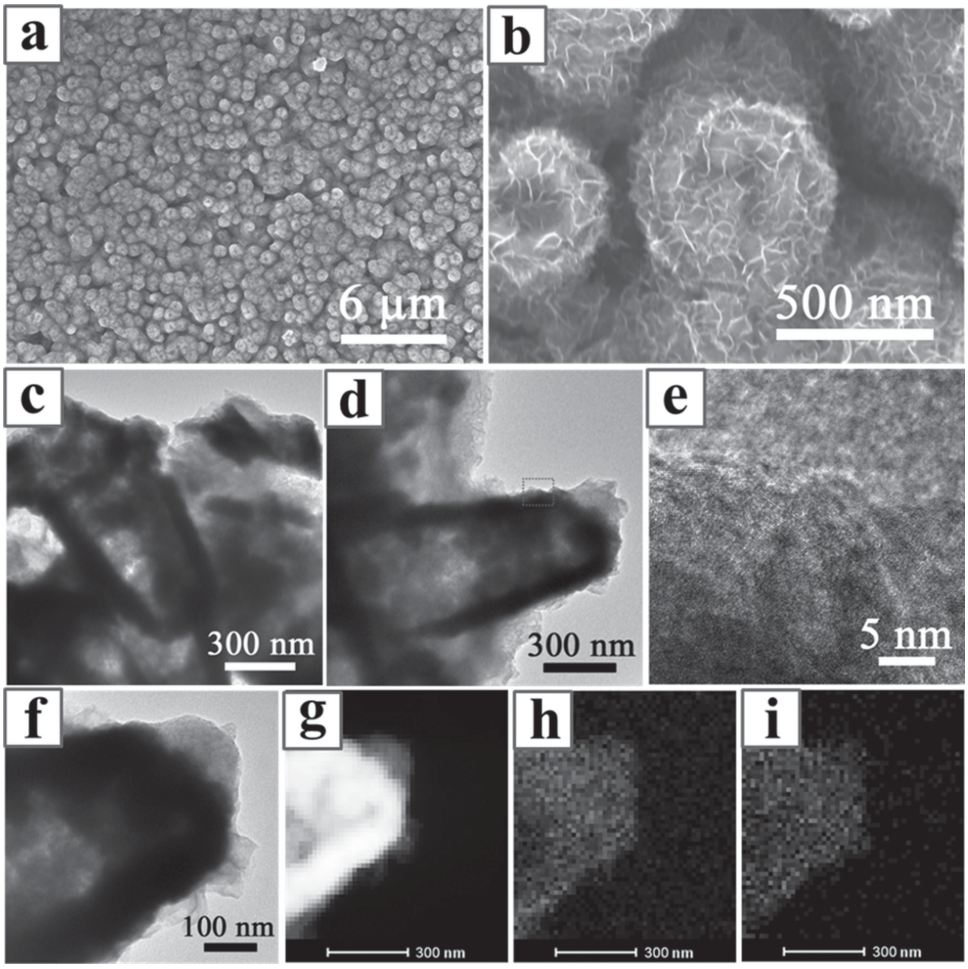

Figure 2. Typical a) low and b) high magnification SEM images of the as-prepared 3D NNCNTAs; c,d,f) TEM images, e) high-resolution TEM (HRTEM) image, g) high-angle annular dark-field TEM (HAADF-STEM) image, and h,i) corresponding EDS elemental mapping images of a fragment of the 3D NNCNTAs: h) Ni, i) Co.

of Ni peaks in binding energies was mainly attributed to the strong electron interactions involving Ni and Co. As expected, when OER is in progress, the electron interactions between Ni and Co may obviously alter the electronic states of Ni atoms and accordingly would improve the catalytic activity and durability of the 3D NNCNTAs. Moreover, it should be noted that the outer $[Ni^{(2+/3+)}Co_2(OH)_{6-7}]_x$ of the 3D NNCNTAs reveals protective effects for NiOOH originated from Ni nanotube "core" materials, which is proved to be a more efficient catalyst for the OER.[7,19] As shown in Figure 3d, the Co 2p spectrum is best fitted with Co^{2+} and two shakeup satellites,[39] which is consistent with that of corresponding O 1s spectrum (Figure 3b and Supporting Information Figure S4). Moreover, for the XRD pattern of the sample shown in Figure S5a (Supporting Information), the diffraction peaks can be indexed to $Ni(OH)_2$ (JCPDF: 14–0117) and $Co(OH)_2$ (JCPDF: 02–0925), indicating that the as-synthesized materials contain a mixture of $Co(OH)_2$ and $Ni(OH)_2$.[38,39,48] The thermogravimertic analysis (TGA) (Supporting Information Figure S5b) further confirms the composition of the sample. Since the atomic ratio of Ni/Co calculated from the XPS result is ≈1:2, the outer materials of the 3D NNCNTAs could be generally expressed as $[Ni^{(2+/3+)}Co_2(OH)_{6-7}]_x$.

To assess the OER catalytic properties, OER electrodes have been investigated in a three-electrode system directly using 3D NNCNTAs as a working electrode and compared with several other electrodes at pH 13 (0.1 M KOH). For comparison, we firstly investigated the effect of ZnO on the OER catalytic activity. As shown in **Figure 4** and **Table 1**, the ZnO@Ni nanorod arrays (ZNNRAs) and NNTAs electrodes exhibit a nearly onset potential at 0.64 V. Remarkably, the NNTAs electrode displays greater OER current and lower Tafel slope, suggesting enhanced OER catalytic activity. We reasoned that ZnO dissolving in the NNTAs electrode mainly contributed to an enhancement in OER catalytic activity compared to the ZNNRAs electrode. On this basis, comparative studies on OER catalytic activity are performed for the 3D NNCNTAs and other electrodes. **Figure 5**a shows their linear sweeps in an anodic direction, from which we can see that the 3D NNCNTAs electrode exhibits a high activity with greater current and earlier onset potential. The onset potential of the catalytic current of the 3D NNCNTAs electrode is about + 0.58 V with a low overpotential (η) of only 0.31 V as compared with that of NNTAs (0.64 V and 0.37 V, respectively). (Table 1, Figure 5). By contrast, it is clear in Figure 5a that bare ITO and ITO-ZnO electrodes do not affect OER activity with poor

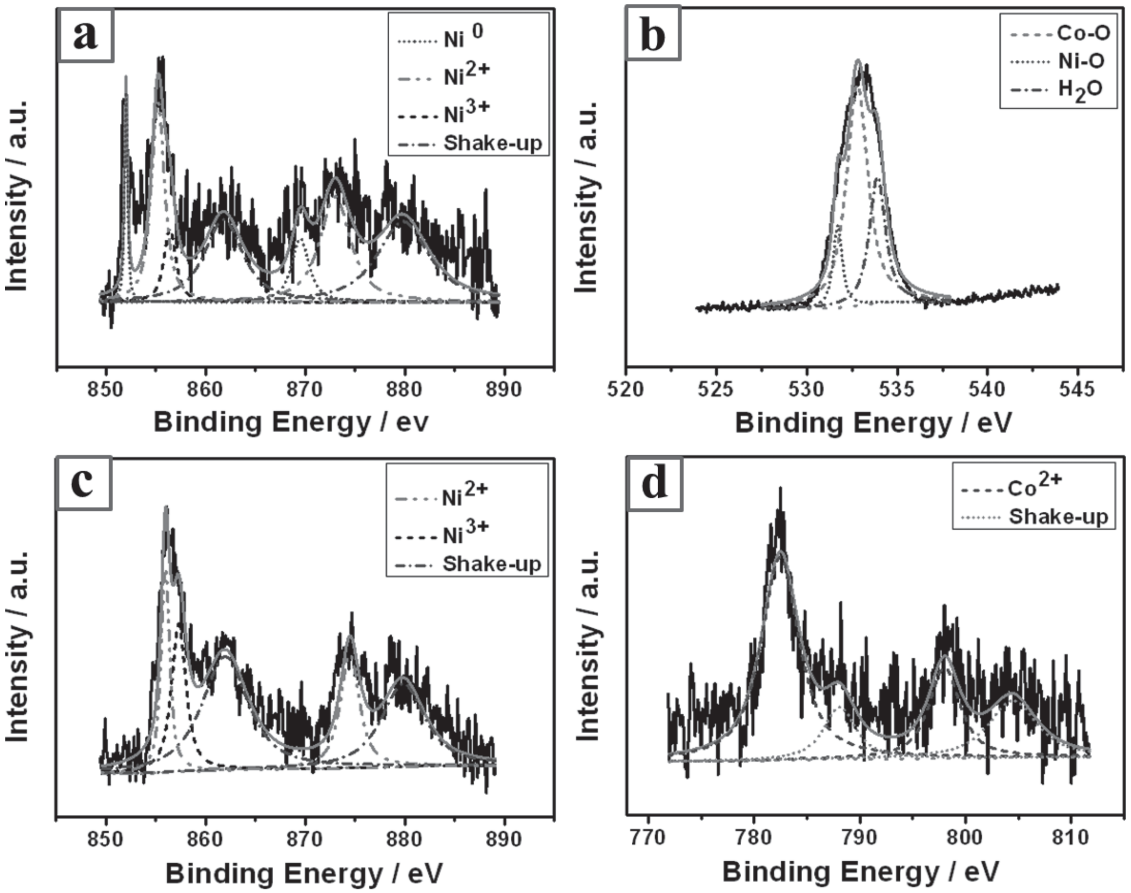

Figure 3. a) Ni 2p XPS of the NNTAs; b) O 1s XPS, c) Ni 2p XPS, and d) Co 2p XPS of the 3D NNCNTAs.

activity. In addition, the high activity is also demonstrated by comparing the current density of the 3D NNCNTA electrode with others, showing that the 3D NNCNTAs electrode explicitly outperforms others over the whole potential range. Note that when the catalytic current of the 3D NNCNTAs electrode reaches 10 mA cm^{-2}, which is a metric relevant to solar fuel synthesis,[20] our 3D NNCNTAs electrode exhibits the enhanced catalytic activity (Table S1, Supporting Information), which can be achieved at a small overpotential of ≈0.46 V, comparable to the performance of the best reported Co_3O_4/graphene catalyst[1] and much greater than the performance of NNTAs electrode (0.66 V). Related with the electron interactions between Ni and Co, the high OER activity of the 3D NNCNTAs electrode may be mainly attributed to CoOOH and NiOOH, which originated from $Ni(OH)_2$ and $Co(OH)_2$. As illustrated in Figure 5a, these peaks of the 3D NNCNTAs and NNTAs curves near 0.25 and

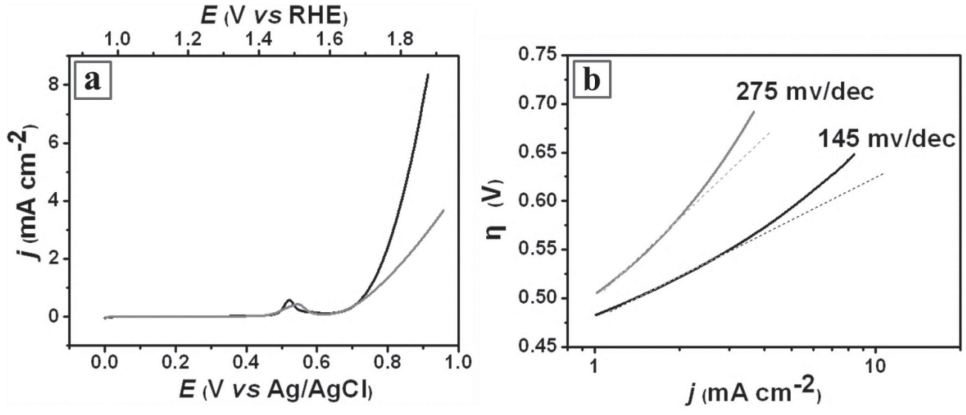

Figure 4. a) iR-corrected polarization curves for OER on the ZNNRAs (gray) and NNTAs (black) electrodes, respectively. b) Tafel plot overpotential versus log(j) derived from (a). All the measurements were performed in O_2-purged 0.1 M KOH (pH ~ 13 at a sweep rate of 5 mV s^{-1}).

Table 1. Electrocatalytic kinetic parameters of the studied electrodes for OER.

Electrode	$E^{a)}$ [V]	$\eta^{c)}$ [V]	$E^{b)}$ [V]	$\eta^{d)}$ [V]	Tafel slope [mV dec^{-1}]
ZNNRAs	0.64	0.37	–	–	275
NNTAs	0.64	0.37	0.93	0.66	145
NNCNTAs	0.58	0.31	0.73	0.46	65

[a)]Onset potential; [b)]Potential at 10 mA cm^{-1}; [c)]Overpotential at onset potential; [d)]Overpotential at 10 mA cm^{-1}.

0. 5 V may be associated with the following mixed reaction of 2, 3, and 4.[39,48,49]

$$Co(OH)_2+OH^- \rightarrow CoOOH+H_2O+e^- \quad (2)$$

$$Ni(OH)_2+OH^- \rightarrow NiOOH+H_2O+e^- \quad (3)$$

$$CoOOH+OH^- \rightarrow 4CoO_2+H_2O+e^- \quad (4)$$

That is to say, in the electrochemical process, $Co(OH)_2$ was first oxidized to CoOOH at about 0.25 V before the oxidation of $Ni(OH)_2$ to NiOOH (≈0.52 V), and then the conductive CoOOH is oxidized to CoO_2 (Co(IV), a more efficient species for the OER)[11,50] at about the same potential of Ni^{2+}/Ni^{3+}, as shown in Figure 5a.

To further evaluate the efficiency of the catalytic reaction from the 3D NNCNTAs electrode, the catalytic kinetics of 3D NNCNTAs and NNTAs was examined with a number of characterizations. Electrical impedance spectroscopy (EIS) performed on 3D NNCNTAs and NNTAs (**Figure 6**a), has similar slopes in the linear part, indicating similar mass transport properties within the electrodes. As compared to NNTAs, the 3D NNCNTAs show a low charge transfer resistance (10.6 Ω for 3D NNCNTA and 28.3 Ω for NNTA) in the high frequency region of the Nyquist plot, corresponding to favourable charge transport kinetics, which may be, to some extent, related with Ni and Co hydroxides redox process.[48,51] Moreover, the electroactive nanostructures are directly attached to the conductive ITO, which avoids the use of other conductive agents and binders, ensures good electrical connection and improves the electroconductivity of the samples and subsequently enhances their electrochemical performance.[43,52–54] On the other hand, Tafel plots are considered with the linear regions fitted into the Tafel equation ($\eta = b \log j + a$, where η is the overpotential, j is the current density, and b is the Tafel slope), plotted in Figure 5b. In comparison with the Tafel slope of NNTAs (145 mV dec^{-1}), the 3D NNCNTAs display a lower Tafel slope of 65 mV dec^{-1}, which further manifest the enhanced kinetics of the 3D NNCNTAs electrode.

Another major concern is the durability of the electrode for OER. As shown in Figure 6b, the as-prepared 3D NNCNTAs electrode exhibits a better activity retaining ability after 1000 cycles. The remarkable features of high activity, favourable kinetics, and strong durability suggest that the as-prepared 3D NNCNTAs electrode is a promising candidate to catalyze OER for water splitting. Further investigations are needed to optimize the OER performance for practical applications, we tentatively attribute the high performance of the system to the following three factors: 1) The unique sandwich-like coaxial structure of the 3D NNCNTAs with the large accessible specific activity area and roughness factor will allow the electroactive species to fully touch the catalyst and efficiently participate in the OER, facilitating the fast intercalation and de-intercalation of active species.[55] 2) Relative to poor electric conductivity in Co_3O_4, this nanostructure ensures improved electronic conductivity owing to the contribution of Ni (Ni^0) nanotube and the electroactive nanostructures that directly attached to the conductive ITO. Furthermore, the discrete hybrid nanotubes directly immobilized to the conductive ITO serve as the current collector, ensures good electrical connection with the conductive ITO, and more importantly, prevents using polymer binder and conductive additives and substantially reduces the electrode "dead volume".[43,52–54] 3) As above mentioned, the synergistic effects originated from electron interactions between Ni and Co mainly alter the electronic states of Ni and Co and accordingly increase the number of electrochemically oxidized tetravalent cations on 3D NNCNTAs surfaces, which would improve the catalytic activity and durability of the 3D NNCTAs electrode.[10,46,47,56]

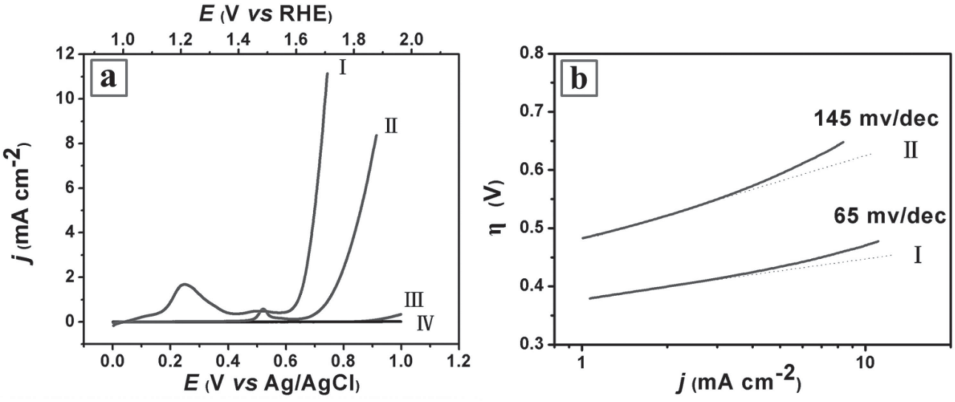

Figure 5. a) iR-corrected polarization curves for OER on a bare ITO electrode (IV) and modified ITO electrodes comprising the ZnO (III), NNTAs (II), and 3D NNCNTAs (I), respectively. b) Tafel plot overpotential versus log(j) derived from (a). All the measurements were performed in O_2-purged 0.1 M KOH (pH = 13 at a sweep rate of 5 mV s^{-1}).

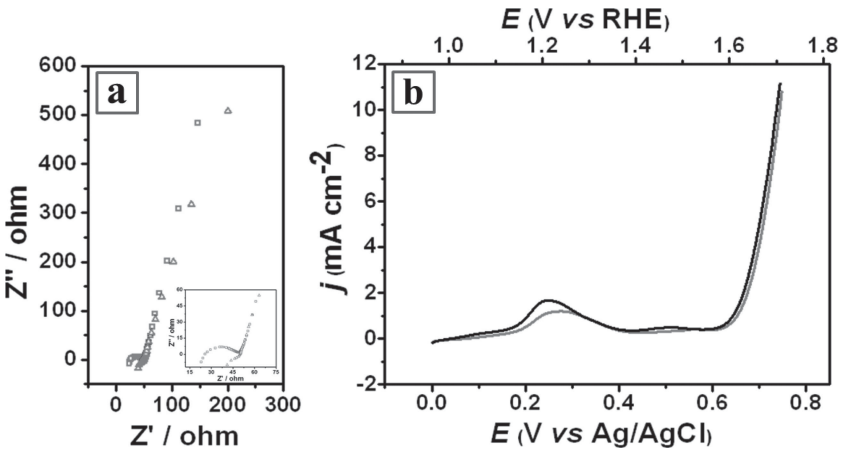

Figure 6. a) EIS of the NNTAs (square) and 3D NNCNTAs (triangle). b) iR-corrected OER polarization curves for the 3D NNCNTAs electrode before (black) and after (grey) 1000 cycles of accelerated stability test.

3. Conclusion

In summary, a binary Ni-Co hydroxide-based sandwich-like coaxial structure of the 3D NNCNTAs is fabricated by a simple electrodeposition method and exploited as a highly effective OER electrode. By taking advantage of the comparatively high surface area, enhanced electron transport, and synergistic effects, the well-designed 3D NNCNTAs electrode exhibits excellent OER electrochemical activity with a small overpotential of ≈0.46 V at the current density of 10 mA cm^{-2}, large anodic currents, and good durability in alkaline medium. It is expected that the structural design of the catalyst will promote the development of OER.

4. Experimental Section

Synthesis of the ZNNRAs Electrode: In a typical synthesis, an ITO electrode (2 cm × 1 cm) was cleaned by sonication for 20 min in acetone, 10% KOH in ethanol, and ultrapure water, respectively.[57] Then, ZnO nanorod arrays modified ITO electrode was fabricated by a simple chronopotentiometry method[46] in solution of 0.01 M $Zn(NO_3)_2$ and 0.05 M NH_4NO_3 with current density of 0.5 mA cm^{-2} at 90 °C for 90 min. After that, ZnO–Ni nanorod arrays electrode was synthesized via the second electrodeposition in solution of 0.02 M $NiSO_4$ and 0.04 M NH_4Cl (pH = 6.0) with current density of 0.35 mA cm^{-2} for 40 min.

Synthesis of the NNTAs Electrode: The NNTAs electrode was obtained by weak acid treatment. The as-prepared ZnO–Ni nanorod arrays were immersed in 0.002 M H_2SO_4 aqueous solution. After dissolving ZnO core in the as-prepared ZnO–Ni nanorod arrays, the NNTAs electrode was prepared.

Synthesis of the 3D NNCNTAs Electrode: The 3D NNCNTAs electrode was prepared by a simple co-electrodeposition process.[43] The as-prepared Ni nanotube arrays were immersed in a solution of 2 mmol of $Ni(NO_3)_2 \cdot 6H_2O$ and 4 mmol of $Co(NO_3)_2 \cdot 6H_2O$, followed by co-electrodeposition at 1.0 V (vs Ag/AgCl) for 12 s.

Material Characterizations: The TEM images were obtained on a JEOL 2010 transmission electron microscope operated at an accelerating voltage of 200 kV equipped with an energy dispersive spectrometer. The XPS measurements were carried out on an ESCALAB-MKII spectrometer (VG Co., UK) with AlKR X-ray radiation as the X-ray source for excitation. The SEM characterizations were performed using a Hitachi S4800 field emission scanning electron microscope operated at 10 kV and a FEI Tecnai F20 transmission electron microscope operated at 200 kV.

Electrochemical Characterizations: Electrochemical measurements (CHI 660e Electrochemical Workstation) were performed in a three electrode electrochemical cell at room temperature using 0.1 M KOH as the electrolyte. The hybrid nanostructure sample electrode (≈0.3 cm^2) acted directly as the working electrode. A Pt coil and Ag/AgCl were used as the counter electrode and the reference electrode, respectively. The current density was normalized to the geometrical area and the measured potentials versus Ag/AgCl were performed with iR compensation enabled and were converted to a reversible hydrogen electrode (RHE) scale according to the Nernst equation.

$$E_{RHE} = E_{Ag/AgCl} + 0.059\ pH + 0.197$$

$$\eta = E_{RHE} - 1.23V$$

Before the electrochemical measurement, the electrolyte (0.1 M KOH, pH ≈ 13) was degassed by bubbling oxygen for 30 min. The accelerated stability tests were performed in O_2-saturated 0.1 M KOH at room temperature by potential cycling between 0.3 and 0.8 V versus Ag/AgCl at a sweep rate of 100 mV s^{-1} for given number of cycles. At the end of each cycling, the resulting electrode was used for polarization curves at a sweep rate of 5 mV s^{-1}.

Supporting Information

Supporting Information is available from the Wiley Online Library or from the author.

Acknowledgements

This work was supported by start-up funds from the Changchun Institute of Applied Chemistry, the Hundred Talents Program of the Chinese Academy of Sciences, and the State Key Laboratory of Electroanalytical Chemistry (no. 110000R387).

Received: January 13, 2014
Revised: February 28, 2014
Published online: April 25, 2014

[1] Y. Liang, Y. Li, H. Wang, J. Zhou, J. Wang, T. Regier, H. Dai, *Nat. Mater.* **2011**, *10*, 780.
[2] J. A. Turner, *Science* **2004**, *305*, 972.
[3] M. D. Symes, L. Cronin, *Nat. Chem.* **2013**, *5*, 403.
[4] M. S. Dresselhaus, I. L. Thomas, *Nature* **2001**, *414*, 332.
[5] J. Xie, H. Zhang, S. Li, R. Wang, X. Sun, M. Zhou, J. Zhou, X. W. Lou, Y. Xie, *Adv. Mater.* **2013**, *25*, 5807.
[6] R. D. L. Smith, M. S. Prévot, R. D. Fagan, Z. Zhang, P. A. Sedach, M. K. J. Siu, S. Trudel, C. P. Berlinguette, *Science* **2013**, *340*, 60.
[7] J. Wang, H.-X. Zhong, Y.-L. Qin, X.-B. Zhang, *Angew. Chem. Int. Ed.* **2013**, *52*, 5248.
[8] M. G. Walter, E. L. Warren, J. R. McKone, S. W. Boettcher, Q. Mi, E. A. Santori, N. S. Lewis, *Chem. Rev.* **2010**, *110*, 6446.
[9] J. Suntivich, K. J. May, H. A. Gasteiger, J. B. Goodenough, Y. Shao-Horn, *Science* **2011**, *334*, 1383.
[10] M. Gong, Y. Li, H. Wang, Y. Liang, J. Z. Wu, J. Zhou, J. Wang, T. Regier, F. Wei, H. Dai, *J. Am. Chem. Soc.* **2013**, *135*, 8452.
[11] B. S. Yeo, A. T. Bell, *J. Am. Chem. Soc.* **2011**, *133*, 5587.

[12] T. Reier, M. Oezaslan, P. Strasser, *ACS Catal.* **2012**, *2*, 1765.
[13] E. Mirzakulova, R. Khatmullin, J. Walpita, T. Corrigan, N. M. Vargas-Barbosa, S. Vyas, S. Oottikkal, S. F. Manzer, C. M. Hadad, K. D. Glusac, *Nat. Chem.* **2012**, *4*, 794.
[14] Y. Li, P. Hasin, Y. Wu, *Adv. Mater.* **2010**, *22*, 1926.
[15] F. Jiao, H. Frei, *Angew. Chem. Int. Ed.* **2009**, *48*, 1841.
[16] M. W. Kanan, D. G. Nocera, *Science* **2008**, *321*, 1072.
[17] R. Subbaraman, D. Tripkovic, K.-C. Chang, D. Strmcnik, A. P. Paulikas, P. Hirunsit, M. Chan, J. Greeley, V. Stamenkovic, N. M. Markovic, *Nat. Mater.* **2012**, *11*, 550.
[18] S. Chen, S.-Z. Qiao, *ACS Nano* **2013**, *7*, 10190.
[19] D. K. Bediako, B. Lassalle-Kaiser, Y. Surendranath, J. Yano, V. K. Yachandra, D. G. Nocera, *J. Am. Chem. Soc.* **2012**, *134*, 6801.
[20] M.-R. Gao, Y.-F. Xu, J. Jiang, Y.-R. Zheng, S.-H. Yu, *J. Am. Chem. Soc.* **2012**, *134*, 2930.
[21] J. Landon, E. Demeter, N. İnoğlu, C. Keturakis, I. E. Wachs, R. Vasić, A. I. Frenkel, J. R. Kitchin, *ACS Catal.* **2012**, *2*, 1793.
[22] J. Del Pilar-Albaladejo, P. K. Dutta, *ACS Catal.* **2013**, *4*, 9.
[23] H. L. He, X. L. Xu, H. X. Wu, Y. D. Jin, *Adv. Mater.* **2012**, *24*, 1736.
[24] Y. D. Jin, X. H. Gao, *Nat. Nanotechnol.* **2009**, *4*, 571.
[25] Y. D. Jin, C. X. Jia, S.-W. Huang, M. O'Donnell, X. H. Gao, *Nat. Commun.* **2010**, *1*, 41.
[26] G. Zhang, H. B. Wu, H. E. Hoster, X. W. Lou, *Energy Environ. Sci.* **2014**, *7*, 302.
[27] G. Zhang, L. Yu, H. B. Wu, H. E. Hoster, X. W. Lou, *Adv. Mater.* **2012**, *24*, 4609.
[28] H. B. Wu, H. Pang, X. W. Lou, *Energy Environ. Sci.* **2013**, *6*, 3619.
[29] X. Liu, S. Shi, Q. Xiong, L. Li, Y. Zhang, H. Tang, C. Gu, X. Wang, J. Tu, *ACS Appl. Mater. Interfaces* **2013**, *5*, 8790.
[30] L. Hu, L. Wu, M. Liao, X. Hu, X. Fang, *Adv. Funct. Mater.* **2012**, *22*, 998.
[31] G. Zhang, B. Y. Xia, X. Wang, X. W. Lou, *Adv. Mater.* **2013**, *26*, 2408.
[32] C. Yuan, H. B. Wu, Y. Xie, X. W. Lou, *Angew. Chem. Int. Ed.* **2014**, *53*, 1488.
[33] G. Zhang, B. Y. Xia, C. Xiao, L. Yu, X. Wang, Y. Xie, X. W. Lou, *Angew. Chem. Int. Ed.* **2013**, *52*, 8643.
[34] T. Grewe, X. Deng, C. Weidenthaler, F. Schüth, H. Tüysüz, *Chem. Mater.* **2013**, *25*, 4926.
[35] S. Guo, S. Zhang, L. Wu, S. Sun, *Angew. Chem. Int. Ed.* **2012**, *51*, 11770.
[36] Y. Liang, H. Wang, P. Diao, W. Chang, G. Hong, Y. Li, M. Gong, L. Xie, J. Zhou, J. Wang, T. Z. Regier, F. Wei, H. Dai, *J. Am. Chem. Soc.* **2012**, *134*, 15849.
[37] Y. Liang, H. Wang, J. Zhou, Y. Li, J. Wang, T. Regier, H. Dai, *J. Am. Chem. Soc.* **2012**, *134*, 3517.
[38] B. Cui, H. Lin, J.-B. Li, X. Li, J. Yang, J. Tao, *Adv. Funct. Mater.* **2008**, *18*, 1440.
[39] C. Shang, S. Dong, S. Wang, D. Xiao, P. Han, X. Wang, L. Gu, G. Cui, *ACS Nano* **2013**, *7*, 5430.
[40] J. Jiang, Y. Li, J. Liu, X. Huang, C. Yuan, X. W. Lou, *Adv. Mater.* **2012**, *24*, 5166.
[41] M. C. Biesinger, B. P. Payne, L. W. M. Lau, A. Gerson, R. S. C. Smart, *Surf. Interface Anal.* **2009**, *41*, 324.
[42] K.-W. Park, J.-H. Choi, B.-K. Kwon, S.-A. Lee, Y.-E. Sung, H.-Y. Ha, S.-A. Hong, H. Kim, A. Wieckowski, *J. Phys. Chem. B* **2002**, *106*, 1869.
[43] C. Yuan, J. Li, L. Hou, X. Zhang, L. Shen, X. W. Lou, *Adv. Funct. Mater.* **2012**, *22*, 4592.
[44] Y. E. Roginskaya, O. V. Morozova, E. N. Lubnin, Y. E. Ulitina, G. V. Lopukhova, S. Trasatti, *Langmuir* **1997**, *13*, 4621.
[45] J. F. Marco, J. R. Gancedo, M. Gracia, J. L. Gautier, E. Ríos, F. J. Berry, *J. Solid State Chem.* **2000**, *153*, 74.
[46] A.-L. Wang, H. Xu, J.-X. Feng, L.-X. Ding, Y.-X. Tong, G.-R. Li, *J. Am. Chem. Soc.* **2013**, *135*, 10703.
[47] V. T. T. Ho, C.-J. Pan, J. Rick, W.-N. Su, B.-J. Hwang, *J. Am. Chem. Soc.* **2011**, *133*, 11716.
[48] J. Li, M. Yang, J. Wei, Z. Zhou, *Nanoscale* **2012**, *4*, 4498.
[49] Y. Tao, L. Zaijun, L. Ruiyi, N. Qi, K. Hui, N. Yulian, L. Junkang, *J. Mater. Chem.* **2012**, *22*, 23587.
[50] G. Mattioli, P. Giannozzi, A. Amore Bonapasta, L. Guidoni, *J. Am. Chem. Soc.* **2013**, *135*, 15353.
[51] M. Oshitani, H. Yufu, K. Takashima, S. Tsuji, Y. Matsumaru, *J. Electrochem. Soc.* **1989**, *136*, 1590.
[52] J. Liu, J. Jiang, C. Cheng, H. Li, J. Zhang, H. Gong, H. J. Fan, *Adv. Mater.* **2011**, *23*, 2076.
[53] C. Yuan, L. Yang, L. Hou, L. Shen, X. Zhang, X. W. Lou, *Energy Environ. Sci.* **2012**, *5*, 7883.
[54] G. Q. Zhang, H. B. Wu, H. E. Hoster, M. B. Chan-Park, X. W. Lou, *Energy Environ. Sci.* **2012**, *5*, 9453.
[55] X. Lu, D. Zheng, T. Zhai, Z. Liu, Y. Huang, S. Xie, Y. Tong, *Energy Environ. Sci.* **2011**, *4*, 2915.
[56] C. Wang, H. Daimon, S. Sun, *Nano Lett.* **2009**, *9*, 1493.
[57] Z. Zhao, G. Zhang, L. Sun, Y. Gao, X. Yang, Y. Li, *Chem. Eur. J.* **2012**, *18*, 5248.